HIGH-RESOLUTION IMAGERY OF URANUS OBTAINED BY STRATOSCOPE II

R.E. Danielson
Princeton University Observatory

and

M.G. Tomasko
Princeton University Observatory and Lunar and Planetary Laboratory, Univ. of Arizona

and

B.D. Savage
Washburn Observatory
University of Wisconsin

Received: _____

June 12, 1972

ABSTRACT

From 17 photographs of Uranus obtained by Stratoscope II, a composite image has been produced having a Gaussian point spread function with a half maximum intensity diameter of 0".2. No certain surface markings are visible. If there are any faint belts parallel to the rotation equator they have a maximum contrast of 5%. The measured limb darkening does not agree with either a deep Rayleigh atmosphere or with clouds high in the atmosphere; a cloud deck under a finite Rayleigh atmosphere seems to be indicated. The equatorial diameter of Uranus is measured to be 51,800 ± 600 km and the ellipticity is estimated to be 0.01 ± 0.01.

I. THE STRATOSCOPE II INSTRUMENT

Stratoscope II was a 36-inch balloon-borne telescope designed for diffraction-limited imagery. A photograph of the instrument as it flew in flights 7 and 8 is shown in Figure 1 and the optical design is shown in Figure 2. Briefly, the f/4 image of the 36-inch (91 cm) diameter primary mirror was magnified by the Gregorian secondary to produce an f/20 image at the field lens. A transfer lens, which provided image stabilization to approximately 0".02 rms, magnified the f/20 image to f/50 (actually f/48.3) at the field mirror where the field of view was 50' in diameter. Finally a Barlow lens produced an f/100 (actually f/105.2) image at the 70 mm camera which photographed a 2' x 2' image. Not shown is a 35 mm camera at f/50 .

More details of the guidance system are given in Figure 3 which shows two optical guidance sensors called retrodividers. Each retrodivider could be commanded to any position in its half of the f/50 plane and had the property that the light from a guide star which was centered on a retrodivider fell equally on each of four photomultipliers. Either retrodivider could be selected to provide the translational error signal; the other retrodivider provided a rotational error signal.

The transfer lens was designed to cancel the coma and astigmatism produced by the primary and secondary mirrors. Therefore the guide star images at the f/50 plane were of high definition. However, some field curvature existed (about 6 mm at the edge of the 64 cm diameter field of view) and therefore a guide star was generally defocussed on the retrodivider apex by about a quarter of a wave since the retrodividers moved in a plane.

Also shown in Figure 3 is the IFA drum, a device which photoelectrically scanned the image of star falling upon it and telemetered it to the ground control station. The telemetered tracing was used to judge the quality of focus and alignment. By remote control, the secondary mirror was adjusted longitudinally to achieve the best focus. Because the transfer lens was slowly cooling during the night, it was necessary to adjust the focus periodically to compensate for the change of focal length of this lens with temperature. No misalignment was detected from the analysis of the output of the IFA device. Consequently, no alignment adjustments were attempted during the flight. However, the stellar images (Figure 8) indicate that some coma due to misalignment may have been present.

The most difficult engineering requirement for diffraction limited imagery in the Stratosphere is keeping the instrument sufficiently isothermal that density variations are not set up in the optical path due to convection in the residual atmosphere. In the Stratoscope II instrument, the optical path in the main tube (up to the f/20 focal plane) was the most sensitive by far. The temperature tolerances are approximately as follows: the main tube and primary mirror temperatures must be uniform and equal to ambient within a tolerance of ± 1°C if the internally generated "seeing" is to be completely negligible. Small portions of the main tube can deviate somewhat more in temperature without disturbing the imagery. The temperature tolerances for the enclosed "side arm" tube are very much larger than for the main tube.

Four separate methods are used to help achieve thermal uniformity. First, the primary mirror was pre-cooled to approximately -50°C and sealed in a mirror cell which was opened after altitude was reached. Second, a

system of heater blankets compensated for radiation losses, chiefly the radiation from the open end of the main tube. Third, low emissivity coatings and radiation shields (see Figure 1) were employed to maintain the circumferential gradients within tolerances. Fourth, the lower portion of the invar main tube was insulated and pre-cooled to ambient temperatures before launch. In this flight, the thermal tolerances were satisfied except for the lower main tube which ran about 4°C warmer than the surroundings.

The instrument was operated by remote control using command, telemetry, and TV systems. The operating range was limited to line-of-sight operation; at 80,000 ft. (24 km) the range is about 500 km. Upon reaching altitude, the telescope was deployed in a series of steps which included unlatching the main tube from the azimuth frame, opening the primary mirror doors, and rotating down to the elevation of the first object. Since the maximum servo torque is less than 10 kg-cm, the 2000 kg telescope had to be balanced to within 2-3 kg-cm before acquisition was possible. Balance was accomplished by adjusting motorized weights. Acquisition was achieved with the aid of two TV cameras employing image orthicons (see Figures 2 and 3). The coarse TV had a field of view of 10° and the fine TV viewed the 50' field of view with the aid of a field mirror located at the f/50 plane. The retrodividers were positioned for each object. The translational guide star was placed on a retrodivider by orienting the telescope to an accuracy of less than 1' with torque commands actuated by a joy stick at the ground control station. Servo lock-on was activated by command upon receiving a "star present" signal via telemetry. Rotational guidance was provided by a gyro which was drift trimmed using error signals generated by the offset of the rotational guide star on the rotational retrodivider.

II. THE RESOLUTION OBTAINED BY STRATOSCOPE II

Figure 8 shows the composite image of a star (SAO 138796 - G5 star of $m_v = 7.9$) taken at very nearly the same focus as the Uranus images. This stellar image (or point spread function) exhibits a central diffraction peak which is somewhat elongated in the vertical direction and which is surrounded by an irregular and incomplete bright ring. Clearly the resolution cannot be described by a single parameter. (Even if the stellar image were symmetric, a single parameter would not suffice.) A complete and very useful description of the resolution is given by the optical transfer function (OTF). This two-dimensional complex function is the Fourier transfer of the point spread function (PSF). The modulus of the OTF is the modulation transfer function (MTF) and gives the reduction of contrast as a function of spatial frequency. Figure 4 shows the MTF determined from the point spread function in Figure 8. For simplicity, only the horizontal (X) and vertical (Y) directions are presented.

For comparison, Fig. 4 also shows the MTF for an ideal 36-inch telescope at 5000Å with the same central obscuration (0.33) as Stratoscope II. The response of a real telescope will be substantially less than ideal even if constructed to superb tolerances. In the case of Stratoscope II, the primary mirror was figured to a surface accuracy of $\frac{\lambda}{50}$ rms which results in a $\frac{\lambda}{25}$ rms wavefront error upon reflection. The secondary mirror was figured to approximately the same accuracy and should produce a similar wavefront error. The enlarging optics (including the folding flat and the field lens) are similarly given an error budget of $\frac{\lambda}{25}$ rms. Taking these sources of error to be independent, they combine quadratically to form a resulting error of $\frac{\lambda}{14}$ rms. Focus errors, alignment errors, and thermal deformations in the

mirror may each be expected to produce a wavefront error of $\frac{\lambda}{25}$ rms (Danielson 1972.) The net result is an rms error of $\frac{\lambda}{10}$ rms which produces a reduction in the MTF similar to that shown in Figure 4. The MTF will be further reduced by the effect of guidance jitter, loss of contrast in the film, and the finite slot size (25μ x 25μ) of the microphotometer. Based on the above tolerance budget, the final MTF of the Stratoscope II system at one-half of the limiting spatial frequency should be about one-half of the MTF of an ideal instrument with an obscuration ratio of 0.33. This MTF, which is closely approximated by an exponential with a 16% response at $\nu = 0.5\ \nu_{lim}$, has been proposed as the practical goal for diffraction limited telescopes operating in the visible (Danielson 1972).

There are several possible reasons why the observed Stratoscope II MTF falls below the design goal. First, some misalignment of the primary and secondary mirrors probably existed which was not detected by the output of the IFA drum. Such misalignment results in an elongated central diffraction maximum and a non-uniform first bright ring, i.e., a coma-like aberration. Second, some quasi-steady air flow patterns were present in the main tube due to lack of perfect temperature uniformity particularly in the lower part of the main tube. Some contribution to the wavefront error was undoubtedly caused by these air patterns, but the magnitude is uncertain. A third possibility is that the primary and secondary mirrors degrade in quality when cooled to -50°C. It was beyond the resources of the SSII Program to construct a facility capable of measuring the figure of the primary mirror while cold.

In spite of the fact that the Stratoscope MTF did not equal the design goal, an extraordinarily high resolution was achieved. Moreover, the instrumental profile was sufficiently stable during the night that it could be determined with adequate precision. In order to demonstrate the resolution that was obtained, the instrumental profile shown in Figure 8 has been averaged in the azimuthal

direction. In Figure 5, it is compared with the profile of a stellar image taken from the surface of the Earth under conditions of good seeing (King 1971). The half maximum diameter of the symmetrically averaged Stratoscope II profile is 0".15 compared with about 1".5 for King's star. The two images are normalized to the same total illuminance on the photographic film.

III. A DECONVOLVED COMPOSITE IMAGE OF URANUS

During Flight No. 7 of Stratoscope II on March 26-27, 1970, 48 photographs were obtained of Uranus at f/100 and 42 at f/50. This paper presents the results of detailed image processing of 17 photographs at f/100 taken on 103 a-G film through a GG-13 filter at the best of the three focus settings. The effective wave length interval was from 3800-5800 Å. The exposure times on these photographs ranged from 5 to 20 sec. Five photographs with 40 sec exposures were excluded from the analysis because of the 0".07 linear blur which occurred due to the motion of Uranus with respect to the guide stars. Table 1 gives the images and exposure times used.

These photographs were digitized with the Sacramento Peak microphotometer. The scanning aperture was a 25 μ square and the stepping length was 25 μ. By means of the photometric calibration curve (described in Section IV), the densities were converted to intensities. Figure 6 shows four original photographs produced from the magnetic tape by a facsimile scanner; the original photographs are reproduced with high fidelity.

No details are apparent on any of the images. In particular no belts or zones are seen parallel to the rotation equator. (The orientation of Uranus in these and subsequent photographs is schematically shown in Figure 7). However, the grain noise in an individual picture is sufficiently large to make faint detail (if present) difficult to detect. (Near the center of the Uranus disk, the mean intensity was about 13 times the rms noise in each pixel.)

In order to reduce the noise, the 17 photographs were registered and averaged by computer. As shown in Figure 8, the resultant composite has much less grain noise; the signal to noise ratio in the composite picture is about 60:1. The increase in the signal to noise ratio is somewhat more than $17^{\frac{1}{2}}$ because some of the noise in the individual photographs is due to scratches and other film defects instead of random noise. Still no surface detail is evident. To be sure, the averaging process would blur out spots smaller than 0".5 due to the rotation of Uranus (the 17 photographs were taken during a 28 minute time interval), but it would leave intact belts and zones parallel to the rotation equator of the type reported by visual observers (Alexander 1965). In any case, it is certain that any features on Uranus are of low contrast, at least in the wavelength interval of these photographs.

In order to set some limits on the contrast of possible belts or zones, the composite shown in Figure 8 has been deconvolved in such a way that the resulting PSF is a symmetric Gaussian. This required an asymmetric two-dimensional convolving function which was produced in the following manner: First, the OTF was computed as the discrete Fourier Transform of the PSF. Because the PSF was contained in a picture consisting of 64 x 64 pixels, the resulting OTF was a 64 x 64 complex matrix. If we denote an individual element of this matrix by T_{ij}, we formed a restoring matrix whose elements were $R_{ij} = T_{ij}^{-1} \Phi_{ij}$. In our case, we chose Φ to be two circularly symmetric Gaussians shown in Figure 9. These values of Φ are the OTF's of the deconvolved photographs. Taking the Fourier Transform of R produced a 64 x 64 convolving function which was necessarily real. To reduce computer time, the final convolution was performed with a 31 x 31 matrix since not all of the 64 x 64 matrix was significantly different from zero.

The results are shown in Figure 8 for Gaussian PSF's having half maximum intensity diameters of 0".25 and 0".20. The PSF's shown were produced by deconvolving the stellar image with the same convolving function used on the averaged Uranus image. The correctness of this procedure is verified by the fact that the PSF's closely approximate the Gaussian shape. It may seem puzzling that the half intensity diameters of the deconvolved Gaussian PSF's in Figure 8 are wider than that of the original symmetrically averaged PSF shown in Figure 5 which has a half intensity diameter of 0".15. The reason for this is that the response of the Gaussian OTF's shown in Figure 9 go to zero at smaller spatial frequencies than the original PSF, particularly in the X direction. Beyond about $0.5\ \nu_{lim}$, the response is so small that one gains more (as a result of suppressing the noise) by eliminating the highest frequency signals than keeping them. The Gaussian OTF was chosen because it amplifies the lower spatial frequencies and suppresses the higher spatial frequencies. Also, the resulting symmetric PSF (of Gaussian shape) is everywhere positive, a very desirable characteristic. It would have been possible to amplify the lower spatial frequencies as much as in the case of the Gaussian OTF's and retain more of the higher frequency response, but the resulting PSF would have contained undesirable negative intensities, i.e. "ringing".

Inspection of Figure 8 reveals no distinct surface markings with the possible exception of some faint belts parallel to the rotation equator. Most (if not all) of the mottling is not real; it is the result of amplifying the lower frequency noise and suppressing the higher frequency noise in the deconvolution. The signal to noise ratio is 26 for the 0".25 Gaussian and 18 for the 0".20 Gaussian PSF's.

We believe that any belts present on Uranus in the 3800 - 5800Å wavelength interval have a contrast no larger than 5%. This conclusion is based on Figure 10

which shows horizontal artificial belts superimposed on the 0".2 deconvolved image. These belts are Gaussian in shape. The centers of the belts are 8%, 4% and 2% darker than the surroundings. The wide belts have a width at half minimum of 0".5 while the narrow belts are 0".25. The 8% belt is readily apparent, the 4% belt is just detectable, and the 2% belt is undetectable. If there are any belts in Figure 8 , their contrast is no larger than 4%. Taking the Gaussian instrumental profiles of the deconvolved images into account, this upper limit becomes a conservative 5%.

IV. PHOTOMETRIC CALIBRATION

The calibration of the Uranus images consisted of two parts. First, since reciprocity effects for our film (103a-G) were small over the range of interest, the central densities of the planet images taken at different exposure times were used to construct a portion of the calibration curve. This was a particularly safe approach as the spectral content of the calibration source and the image source were automatically identical, thereby eliminating any effects due to a variation of gamma with wavelength. Second, several calibration wedges were placed on a sample of unexposed film and developed in the same way (but not in the same batches) as the Uranus photographs. Film samples were also exposed in the calibration box without the plastic Kodak step wedge in order to establish the uniformity of illumination on the wedge.

The diffuse densities of the steps of the plastic step wedge were determined with an error $\leq$ 2% by comparison with a calibrated Kodak step tablet on a McBeth "Quantalog" opal densitometer. When combined with the data on the uniformity of illumination of the light box, the intensities producing the steps of the film wedge copies were fixed with errors $\leq$ 3%.

After microphotometry of each image of Uranus, one of the calibration

wedges was scanned to calibrate any drift in the microphotometer. No perceptible change in scale factor occurred during the digitizing session, but a small zero point drift of the microdensitometer was observed. In light of this and the fact that the fog level varied slightly between batches, the mean digitized fog density was determined for each Uranus frame. The difference between the fog value for a frame and a "standard" fog value was subtracted from the recorded densities. The central Uranus density was obtained by averaging over a central square equal to 1/8 of the diameter on a side; the surface brightness was sensibly flat over this area.

The mean adjusted central densities for the different exposure times are shown plotted separately in the insert of Figure 11 for the two development batches. The vertical bars indicate the extreme members in an exposure group while the numbers to the right of the curves give the number of images in the group. Telemetry data confirmed that the exposure times were accurate. Since only relative intensities are required for this paper, the smooth curve defined by horizontally shifting the mean points from one of the development batches a fixed amount (in log I) was adopted as the relative calibration over this nearly linear region.

Each of the calibration wedges differed slightly, but fortunately one was found to match the Uranus center data extremely well. This wedge curve was used to define the low intensity portion of the adopted calibration curve, shown in Figure 11.

As a check on the accuracy of the calibration, separate limb darkening curves were produced in the equatorial direction for the average of the 5, 10, and 20-second exposures. The shapes of these three curves (shown in Figure 13) are in good agreement generally differing from the mean value by less than $\pm$ 3%.

V. LIMB DARKENING CURVES

The lack of any certain surface marking makes it easier to measure the limb darkening and to compare it with theoretical models. One question which might be answered from such a comparison is whether the upper cloud deck on Uranus is at the top of the atmosphere or whether it lies deep in the atmosphere. In the latter case (Belton, et. al.1971), the observed limb darkening curve should be that due to Rayleigh scattering. In the former case, the observed curve would mainly be the result of scattering by cloud particles, and one might expect agreement with the limb darkening predicted by phase functions characteristic of clouds, e.g. the Henyey-Greenstein phase functions.

Figure 12 shows four different limb darkening curves, each of which has a geometric albedo of about 0.5. They were computed for zero phase to match the conditions of observation (within a few hours of opposition). The curve for Henyey-Greenstein scattering is for the semi-infinite case and was computed by Hansen (1971). The curve for non-conservative Rayleigh scattering is also for the semi-infinite case and was calculated using the H functions of Abhyankar and Fymat (1971). The curve for finite conservative Rayleigh scattering over a Lambert surface was calculated using the X and Y functions of Sekera and Kahle (1966). The geometric albedo which is a mean for the 3800-5800Å bandpass was taken from Younkin (1970) corrected to an equatorial radius of 25,900 km (see section VI).

The theoretical and observed limb darkening curves were compared in the following manner. First, the average of 9 scanning lines centered about the equatorial direction was computed. (The true diameter of Uranus is approximately 77 lines). Second, artificial images of Uranus were computed

which obeyed the limb darkening laws shown in Figure 12. These images were convolved with the PSF and a similar average of 9 lines was taken. The resulting theoretical curves were fit to the observed curve by normalizing the central brightness and by adjusting the diameter of the original artificial image so that the curves coincided near and beyond the true limb. The shapes of the different curves beyond the true limb are similar because they are mainly a result of the instrumental function.

Figure 13 compares the two extreme theoretical limb darkening curves with the observed limb darkening curves based on the averages of the 5, 10 and 20 second exposures. The differences between the observed curves are indicative of the systematic errors in the photometric correction; the close agreement is encouraging. It is evident that neither the very thick Rayleigh atmosphere nor the Henyey-Greenstein atmosphere fits the data closely.

The average of all 17 exposures is compared with all four theoretical curves in Figure 14. It is interesting to note that a Lambert surface is in better agreement than Rayleigh or Henyey-Greenstein scattering. No special significance is attached to this fact except it does suggest that the upper atmosphere of Uranus may be intermediate between the two limiting cases in Figure 13. The only intermediate cases for which we have computed limb darkening curves have conservative Rayleigh atmospheres overlying gray Lambert surfaces. The best fit to the data has a Rayleigh atmosphere of $\tau = 0.5$ overlying a Lambert surface of albedo 0.75. This model has a geometric albedo of approximately 0.59. Figure 15 shows that this intermediate case also fits the data very well in the polar direction.

The preceding analysis is, of course, vulnerable to systematic errors since small differences in relative intensity are involved. We do not believe that systematic errors in the PSF affect our results for several reasons. First, individual photographs of the comparison star are very similar at the same focus setting indicating that the PSF was quite steady during the time that the Uranus photographs were taken. Second, the focus setting for the comparison stars differed by only a quarter wave from the focus setting for the Uranus photographs. This amount of focus change produced a negligible change in the observed PSF. Third, the spectral type of the comparison star (G5) is similar to the sun, thereby minimizing any differential color effects between the PSF and Uranus. Fourth, the PSF is sufficiently small compared with Uranus that it has a negligible effect on the theoretical limb darkening curves out to one-half of the radius of the limb, i.e. within about one arc second from the center of the disk. Thus comparisons of the theoretical and observational curves at this radius are quite insensitive to the PSF. The most vulnerable source of systematic error is the photometric calibration which is described in detail in section IV. On the basis of this discussion plus the three sets of data shown in Figure 13, we feel that the photometric calibration is accurate enough to rule out the two extreme theoretical curves in Figure 13.

VII. THE DIAMETER AND ELLIPTICITY OF URANUS

The precise knowledge of the instrumental function plus the good fit of the Rayleigh-Lambert model in Figure 14 makes it possible to make a fairly accurate determination of the equatorial diameter of Uranus. When converted

to dimensions on the film, the result is D_{eq} = 1.92 ± 0.02 mm. The error is an estimate of the uncertainty in fitting the Rayleigh-Lambert composite model to the data. Combined with the plate scale (2.146 ± 0.005 "/mm) the apparent angular diameter is 4".12 ± 0".04. Since Uranus was 17.32 a.u. from the Earth at the time of exposure, the linear equatorial diameter equals 51,800 ± 600 km. Converted to 19.19 a.u., the angular diameter is 3".72 ± 0".04.

From Figure 15, the measured polar diameter D_{pol} = 1.91 ± 0.02 mm which is only very slightly smaller than the equatorial diameter. However, during the time of exposure, Uranus moved in the polar direction with respect to the guide stars at a rate of about 0".0018/sec. This has not been taken into account in the image processing, but the maximum elongation in the polar direction during a 14 second exposure (the average length of the 17 exposures) was 0".025 or 0.006 of the polar diameter. The best we can conclude is that the ellipticity $\epsilon = (D_{eq} - D_{pol}) / D_{eq}$ is 0.01 ± 0.01. Correction for the latitude of the center of the disk, approx. 20°, does not significantly affect this result.

An important potential source of systematic error in determining the equatorial diameter of Uranus is the plate scale. Based on the optical parameters of the Stratoscope II instrument, the plate scale is 2".145 /mm. This is in agreement with the value obtained by Light (1971) based on the measured equatorial diameter of Jupiter obtained on the same flight. This measurement yielded 2.145 ± 0.005 "/mm and was based on the equatorial and polar diameters of Jupiter given by Dollfus (1970). A second determination was based on the distance between Jupiter and Io on a series of photographs

when Io was undergoing eclipse. This yielded 2.150 ± 0.011 " /mm. We therefore believe that our plate scale is not the major factor determining the errors in the polar and equatorial diameters.

VIII. DISCUSSION OF RESULTS

The agreement of the limb darkening data with the finite (τ = 0.5) Rayleigh atmosphere suggests a model of roughly 130 km-atm of H_2 over the upper cloud deck. This amount of H_2 has an optical thickness of 0.5 at 5000Å, the center of the band pass. Interestingly, this H_2 abundance is of the same order as is predicted to occur above the methane cloud deck in some atmospheric models we have produced. These models are being studied in a separate investigation.

The derived value of the equatorial diameter (51,800 ± 600 km) is in excellent agreement with the value of 50,800 ± 560 km obtained by Dollfus (1970) based on the double image micrometer. The derived value of the ellipticity (0.01 ± 0.01) is consistent with the value ϵ = 0.030 ± 0.008 obtained by Dollfus.

Based on a mass of 14.5 times the mass of the Earth, the Stratoscope results yield 1.21 ± 0.04 gm/cm^3 as the mean density of Uranus. Previous models of the interior of Uranus (Reynolds and Summers 1965) based on a mean density of 1.6 gm/cm^3, concluded that the bulk of Uranus must consist of heavier substances than H_2 and He. Although these conclusions need re-examination in light of the new density, the calculations of Zapolsky and Salpeter (1969), strongly indicate that even with the reduced density, Uranus contains a higher proportion of heavier elements than does Jupiter or Saturn.

ACKNOWLEDGEMENTS

The successful flight of Stratoscope II was critically dependent on the extraordinary efforts of the engineers of the Perkin-Elmer Corporation who prepared the instrument for flight, the engineers of the Vitro Corporation who launched the instrument, and the engineers of RCA who maintained the vital television links. Invaluable support was provided by the personnel of the NCAR Scientific Balloon Flight Station during field testing and during launch. The photographic images of Uranus and the comparison stars were digitized using the microphotometer at Sacramento Peak Observatory; the extraordinary assistance and cooperation of its staff is gratefully acknowledged. Dr. E. S. Light assisted in the microphotometry. Special thanks are due to Dr. James Hansen for computing the Henyey-Greenstein limb darkening curves. We thank Dr. A. L. Fymat for sending us his H functions in convenient computer card form. Part of the data analysis was supported by NSF Grant GP 23580. The image processing techniques, which were in part based on the JPL VICAR system, were developed under NASA Grant NGR-31-001-142. Project Stratoscope is sponsored by NASA Grant NGR 31-001-001.

TABLE 1

Images Comprising the Uranus Average

Exposure Number	Exposure Time
98	10 sec
99	20
100	20
116	5
117	20
118	10
119	10
121	20
122	20
123	6
125	20
126	20
127	10
128	5
130	20
131	10
132	5

REFERENCES

Abhyankar, K.D., and Fymat, A.L. 1971, Ap.J. Supp., 23, 35.

Alexander, A.F. O'D. 1965, The Planet Uranus (London: Faber & Faber).

Belton, M.J.S., McElroy, M.B., and Price, M.J. 1971, Ap.J, 164, 191.

Danielson, R.E., 1972, Proc. Am. Astronaut. Soc. (In press).

Dollfus, A., 1970, Icarus, 12, 101.

Hansen, J.E., 1971, private communication.

King, I.R., 1971, Pub. A.S.P., 83, 199.

Light, E.S., 1971, private communication.

Reynolds, R.T. and Summers, A.L., 1965, J. Geophys. Res., 70, 199.

Sekera, K. and Kahle, A., 1966, Report R-452-PR (Santa Monica, California: Rand Corp.).

Younkin, R.L. 1970, Spectrophotometry of the Moon, Mars, and Uranus (Ph.D. Thesis: UCLA).

Zapolsky, H.S. and Salpeter, E.E. 1969, Ap.J., 158, 809.

FIGURE CAPTIONS

Fig. 1. - Stratoscope II in the configuration of Flights 7 and 8.

Fig. 2. - Optical diagram of Stratoscope II.

Fig. 3. - Detailed optical diagram of the "side arm".

Fig. 4. - The modulation transfer function (MTF) is shown for two ideal 36-inch telescopes and for a 36-inch telescope operating to the Stratoscope II error budget. The actual MTF of Stratoscope II is shown in two perpendicular directions in frequency space.

Fig. 5. - Comparison of the symmetrically averaged Stratoscope II instrumental function with that published by King (1971).

Fig. 6. - Four original images of Uranus.

Fig. 7. - Schematic orientation of Uranus in Figures 6, 8 and 10.

Fig. 8. - The upper photographs show the average of the 17 Uranus images listed in Table 1 along with the average of a star taken at very nearly the same focus setting. The middle photographs show Uranus deconvolved to a Gaussian point spread function (PSF) with a half maximum intensity diameter of 0".25 along with the PSF. The lower photographs are similar except the half maximum diameter of the PSF is 0".20.

Fig. 9. - Transfer functions showing the degree of amplification of spatial frequencies in the deconvolutions shown in Figure 8.

Fig. 10. - Horizontal artificial belts of Gaussian shape have been superimposed on the 0".2 deconvolved images. The darkest portions of the belts are 8%, 4% and 2%. The widths of the belts are at half maximum darkness.

Fig. 11. - The photometric calibration curve.

Fig. 12. - Theoretical limb darkening curves. The Rayleigh scattering is true Rayleigh scattering, not the Rayleigh phase function. ω_0 is the single scattering albedo. g is the average of the Henyey-Greenstein phase function over cos θ. A is the Lambert surface albedo.

Fig. 13. - Comparison of Rayleigh scattering and Henyey-Greenstein limb darkening curves (blurred with the instrumental function) with the observed limb darkening curves based on the averages of the 5, 10 and 20 second exposures of Uranus. The difference between the observed curves is a measure of the systematic errors in the photometric corrections.

Fig. 14. - Comparison of the four theoretical limb darkening curves in Figure 12 (blurred with the instrumental function) with the observed limb darkening curve based on the average of all 17 Uranus images.

Fig. 15. - The best fitting theoretical curve in Figure 14 is compared with the observed limb darkening curve in the polar direction.

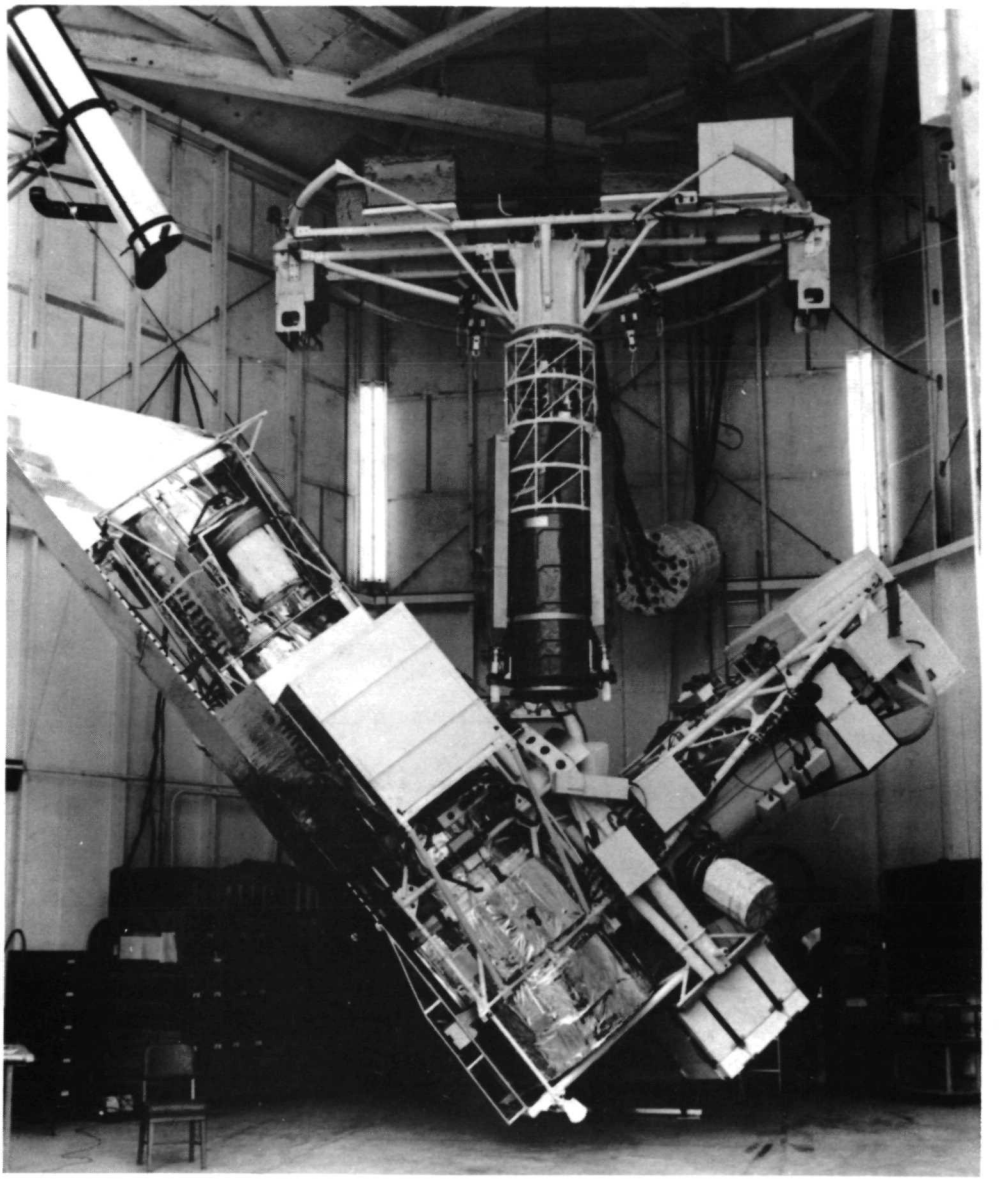

Fig. 1

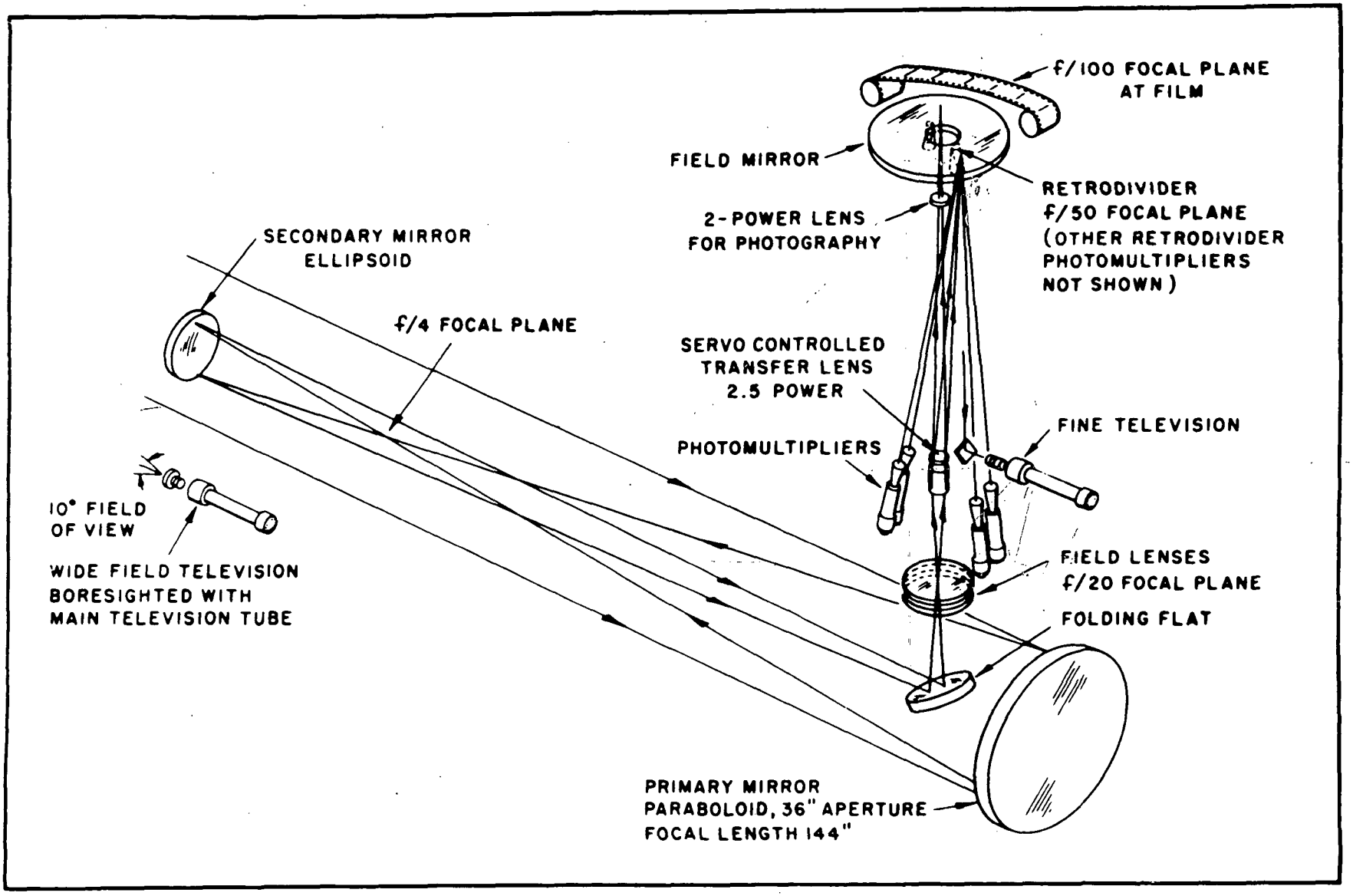
f/100 FOCAL PLANE
AT FILM
FIELD MIRROR
RETRODIVIDER
f/50 FOCAL PLANE
(OTHER RETRODIVIDER
PHOTOMULTIPLIERS
NOT SHOWN)
2-POWER LENS
FOR PHOTOGRAPHY
SECONDARY MIRROR
ELLIPSOID
f/4 FOCAL PLANE
SERVO CONTROLLED
TRANSFER LENS
2.5 POWER
FINE TELEVISION
PHOTOMULTIPLIERS
10° FIELD
OF VIEW
WIDE FIELD TELEVISION
BORESIGHTED WITH
MAIN TELEVISION TUBE
FIELD LENSES
f/20 FOCAL PLANE
FOLDING FLAT
PRIMARY MIRROR
PARABOLOID, 36" APERTURE
FOCAL LENGTH 144"

Fig. 2

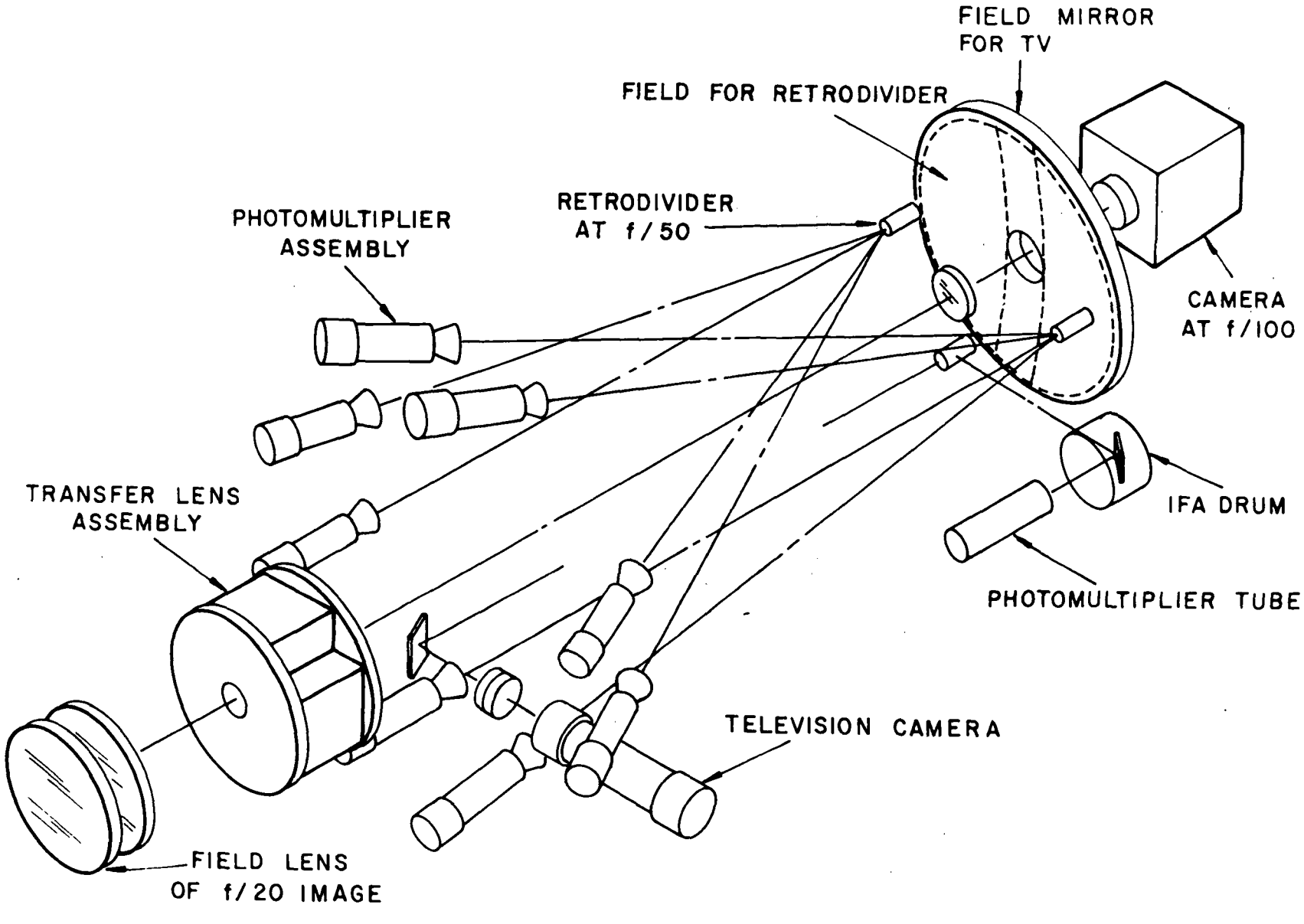
FIELD MIRROR
FOR TV
FIELD FOR RETRODIVIDER
RETRODIVIDER
AT f/50
PHOTOMULTIPLIER
ASSEMBLY
CAMERA
AT f/100
TRANSFER LENS
ASSEMBLY
IFA DRUM
PHOTOMULTIPLIER TUBE
TELEVISION CAMERA
FIELD LENS
OF f/20 IMAGE

Fig. 3

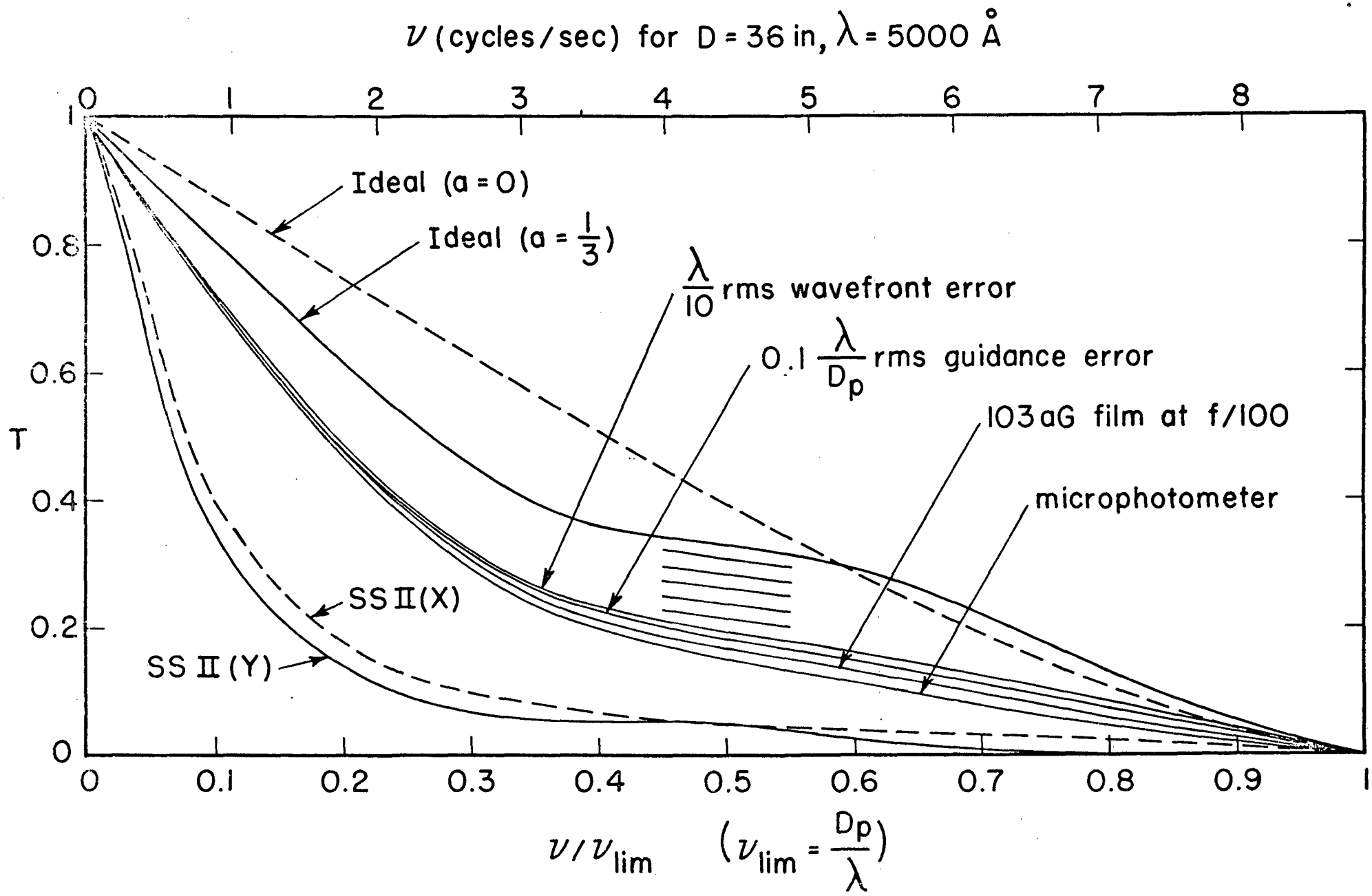
ν (cycles/sec) for D = 36 in, λ = 5000 Å
0
1
2
3
4
5
6
7
8
Ideal (a = 0)
Ideal (a = 1/3)
λ/10 rms wavefront error
0.1 λ/Dp rms guidance error
103aG film at f/100
microphotometer
SS II(X)
SS II(Y)
T
0
0.2
0.4
0.6
0.8
1
0
0.1
0.2
0.3
0.4
0.5
0.6
0.7
0.8
0.9
1
ν/ν lim
(ν lim = Dp/λ)

Fig. 4

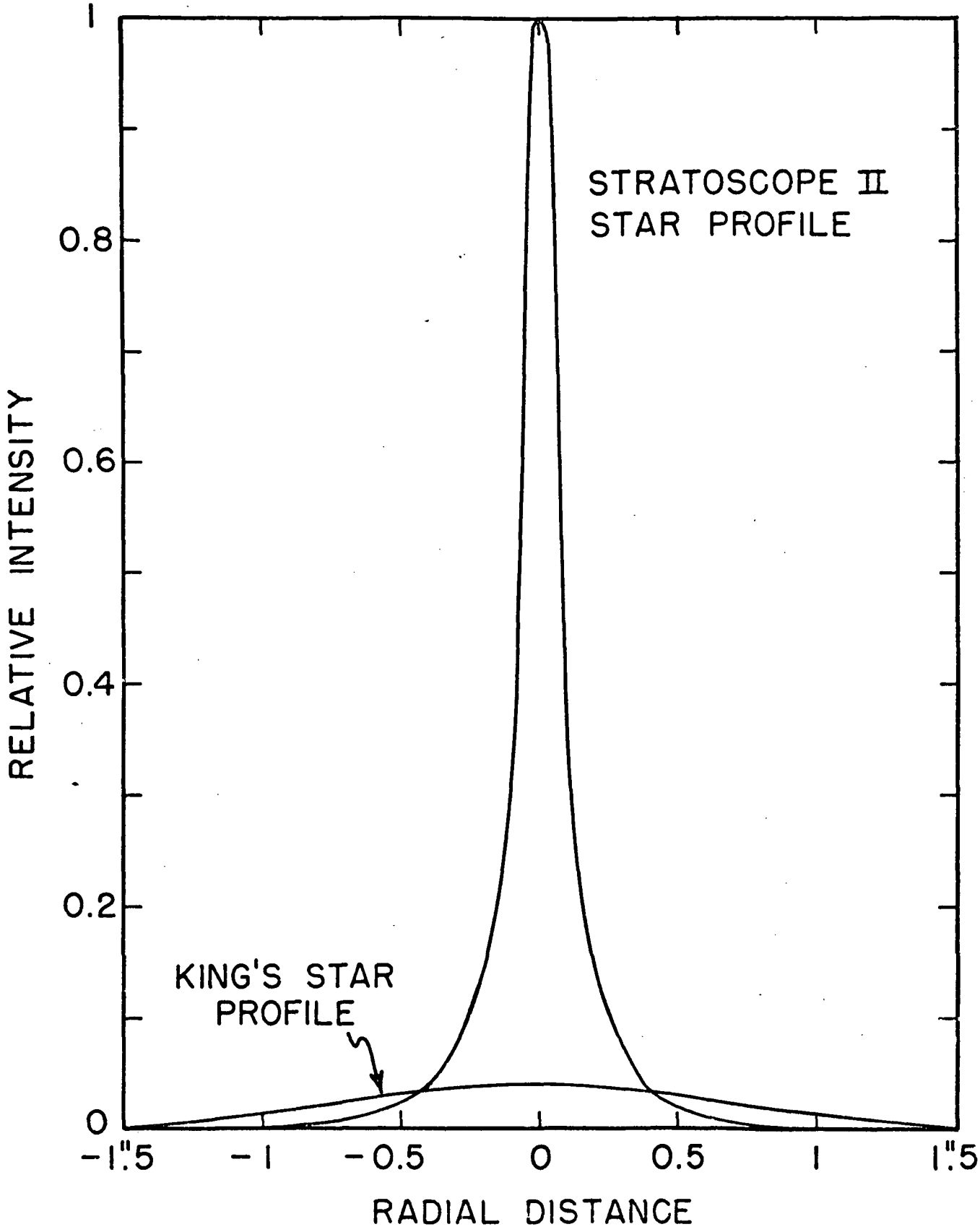
STRATOSCOPE II
STAR PROFILE
KING'S STAR
PROFILE
RELATIVE INTENSITY
1
0.8
0.6
0.4
0.2
0
-1".5
-1
-0.5
0
0.5
1
1".5
RADIAL DISTANCE

Fig 5

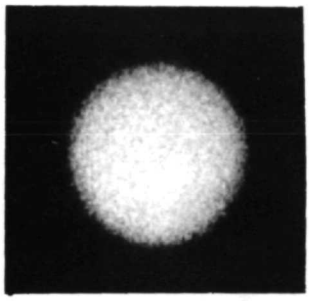

98

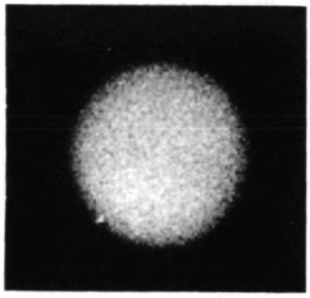

99

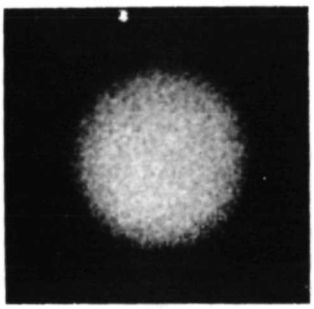

116

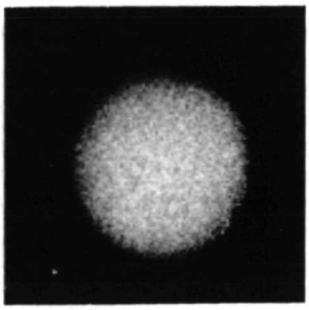

118

Fig. 6

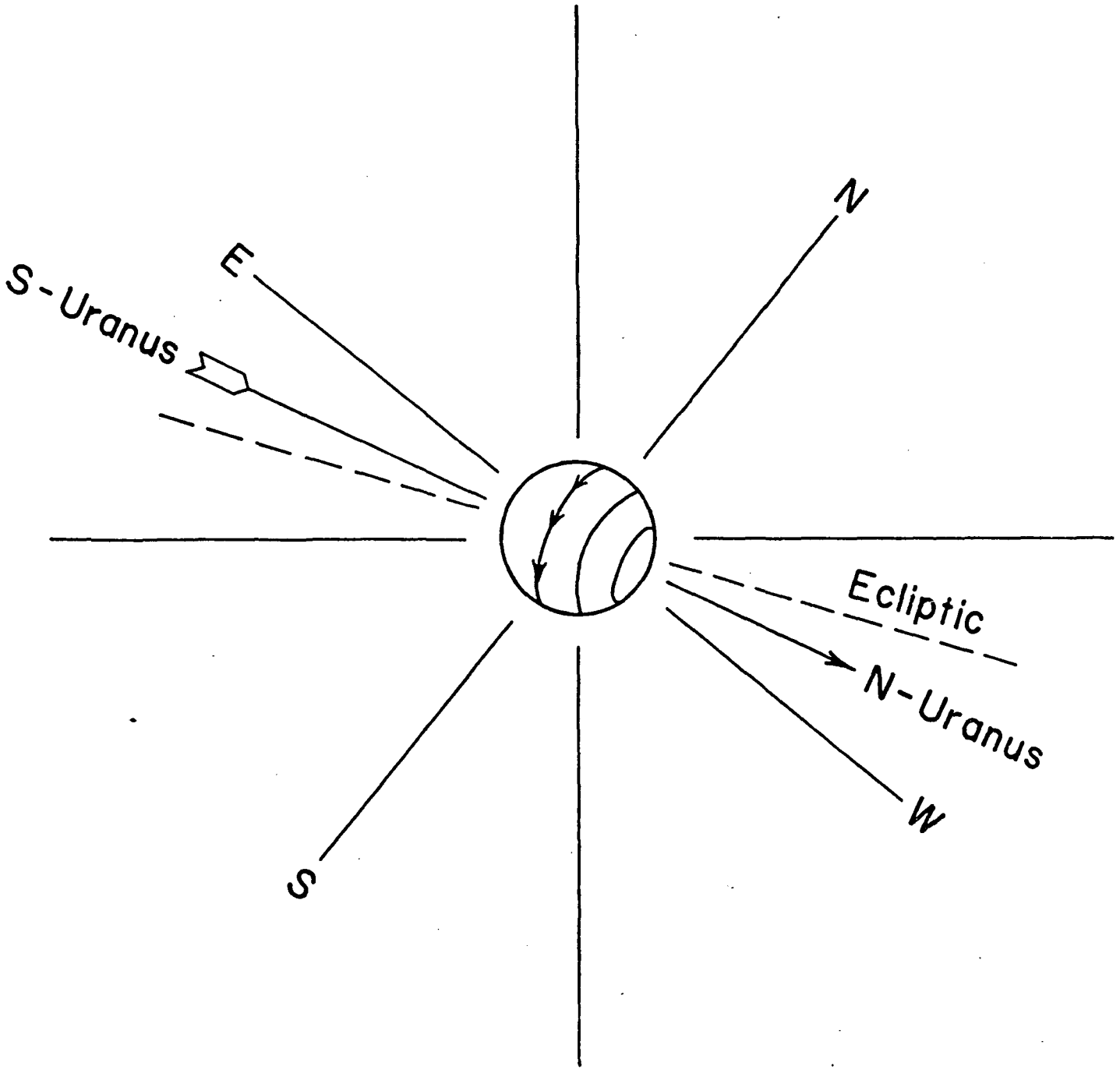

Fig 7

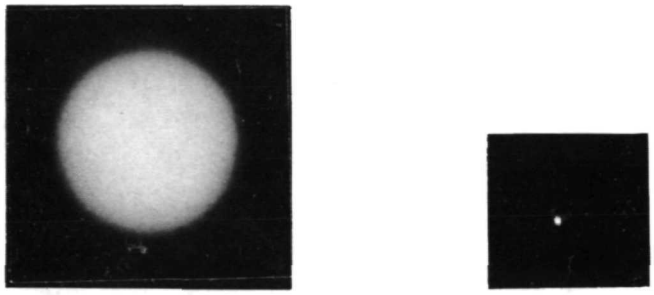

Average of 17 Photographs

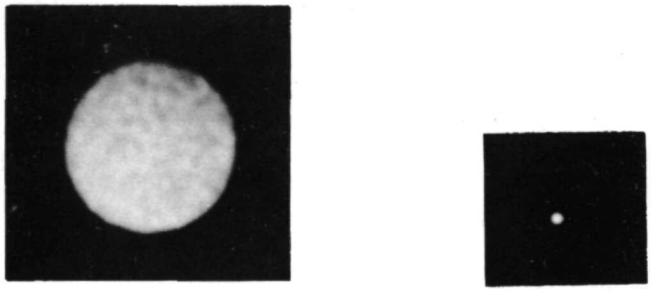

Deconvolved to 0".25 PSF

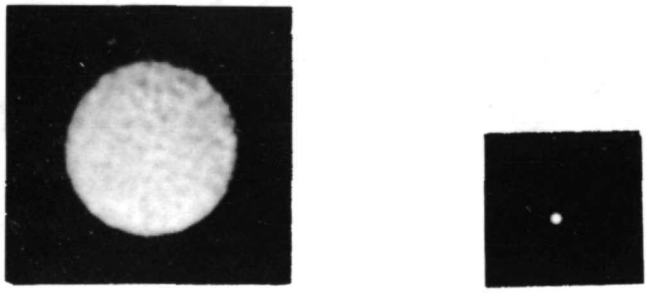

Deconvolved to 0".20 PSF

Fig. 8

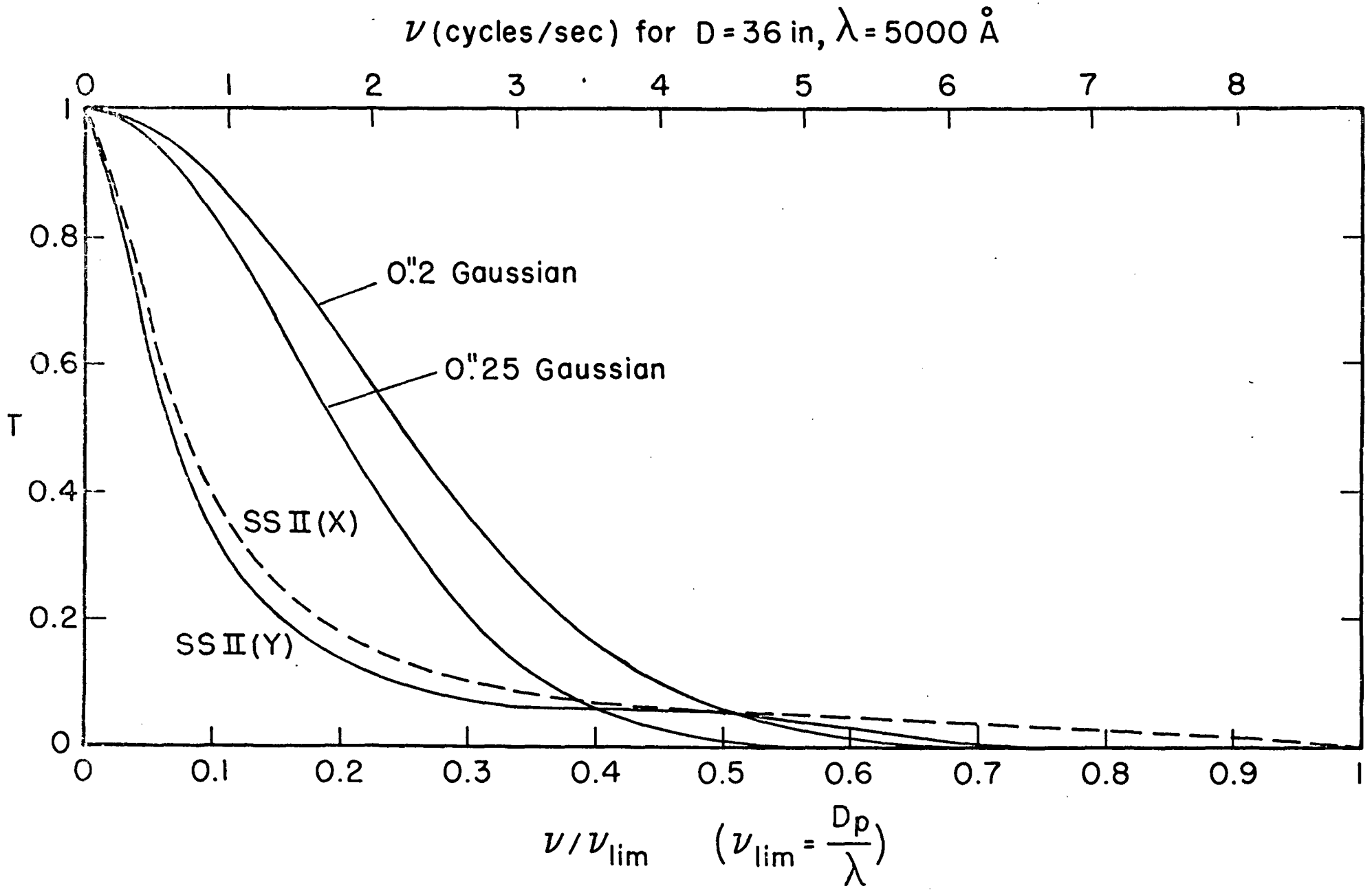
ν (cycles/sec) for D = 36 in, λ = 5000 Å
0
1
2
3
4
5
6
7
8
1
0.8
0.6
0.4
0.2
0
T
0".2 Gaussian
0".25 Gaussian
SS II (X)
SS II (Y)
0
0.1
0.2
0.3
0.4
0.5
0.6
0.7
0.8
0.9
1
ν / ν lim
(ν lim = Dp/λ)

b 719.

0".5 Gaussian Belts

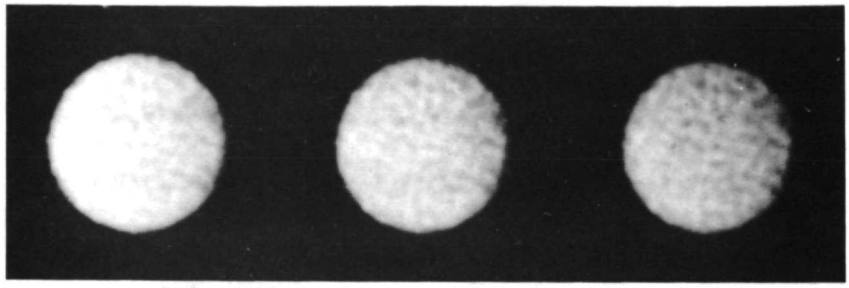

8% 4% 2%

0".25 Gaussian Belts

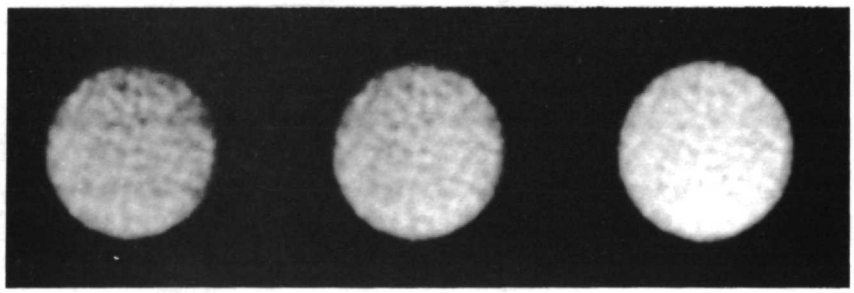

8% 4% 2%

Fig. 1
10

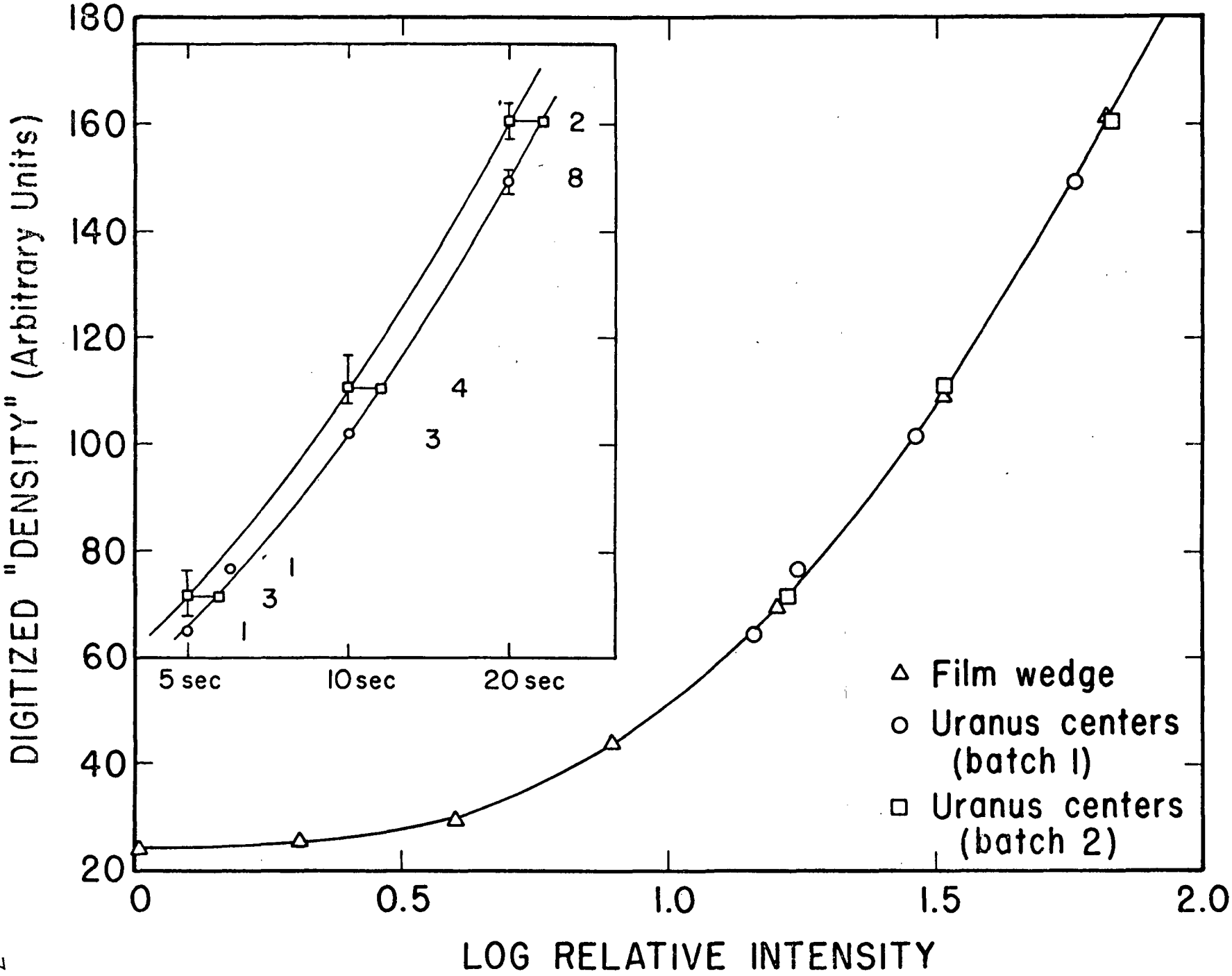
DIGITIZED "DENSITY" (Arbitrary Units)
LOG RELATIVE INTENSITY
180
160
140
120
100
80
60
40
20
0
0.5
1.0
1.5
2.0
5 sec
10 sec
20 sec
1
2
3
4
8
Film wedge
Uranus centers (batch 1)
Uranus centers (batch 2)

Fig. 11

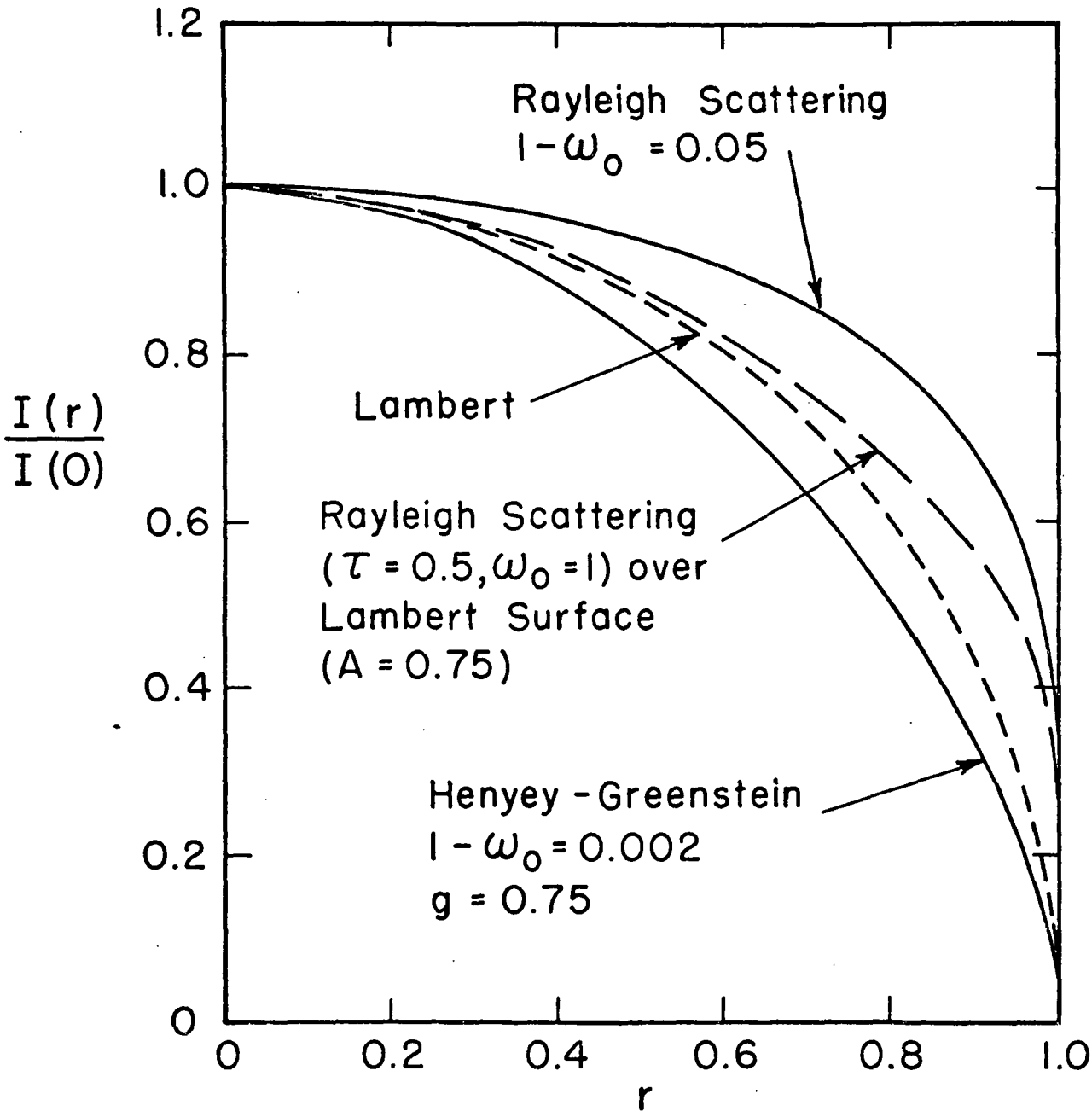
1.2
1.0
0.8
0.6
0.4
0.2
0
I(r)/I(0)
Rayleigh Scattering
1-ω0 = 0.05
Lambert
Rayleigh Scattering
(τ = 0.5, ω0 = 1) over
Lambert Surface
(A = 0.75)
Henyey-Greenstein
1 - ω0 = 0.002
g = 0.75
0
0.2
0.4
0.6
0.8
1.0
r

fig 12

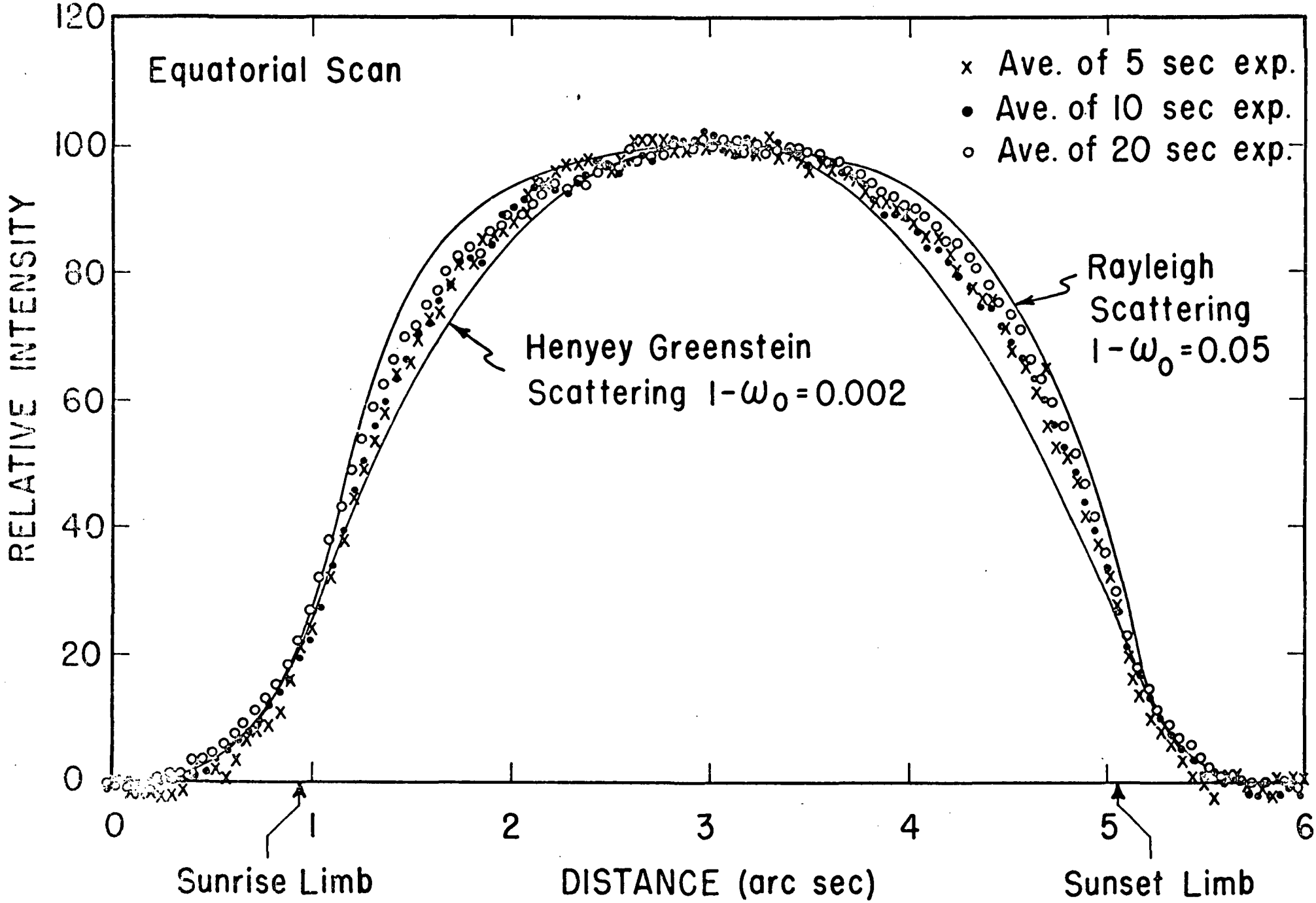
Equatorial Scan
x Ave. of 5 sec exp.
• Ave. of 10 sec exp.
o Ave. of 20 sec exp.
Rayleigh Scattering $1-\omega_0=0.05$
Henyey Greenstein Scattering $1-\omega_0=0.002$
RELATIVE INTENSITY
120
100
80
60
40
20
0
0
1
2
3
4
5
6
Sunrise Limb
DISTANCE (arc sec)
Sunset Limb

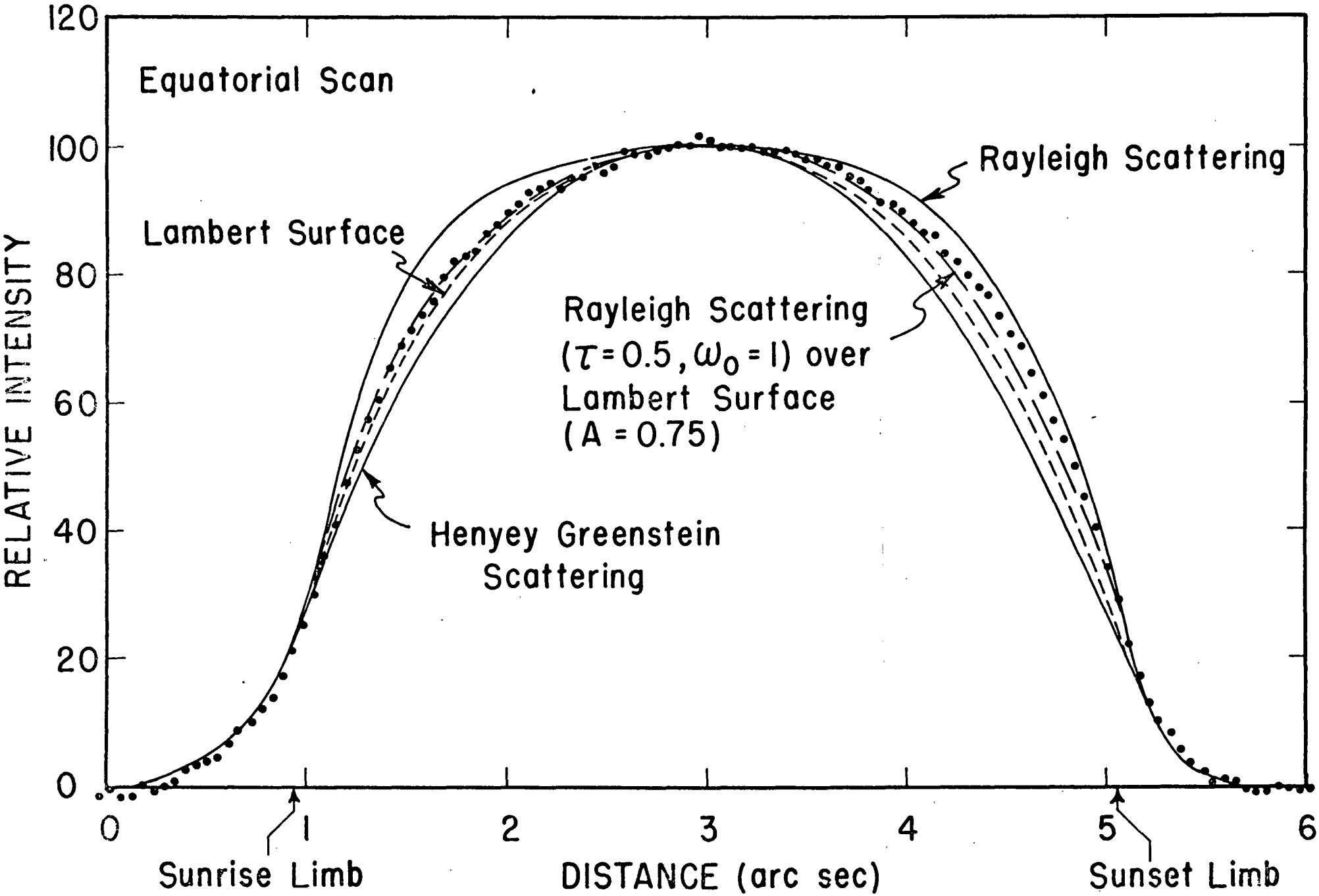
Equatorial Scan
Rayleigh Scattering
Lambert Surface
Rayleigh Scattering
(τ = 0.5, ω0 = 1) over
Lambert Surface
(A = 0.75)
Henyey Greenstein
Scattering
RELATIVE INTENSITY
120
100
80
60
40
20
0
0
1
2
3
4
5
6
Sunrise Limb
DISTANCE (arc sec)
Sunset Limb

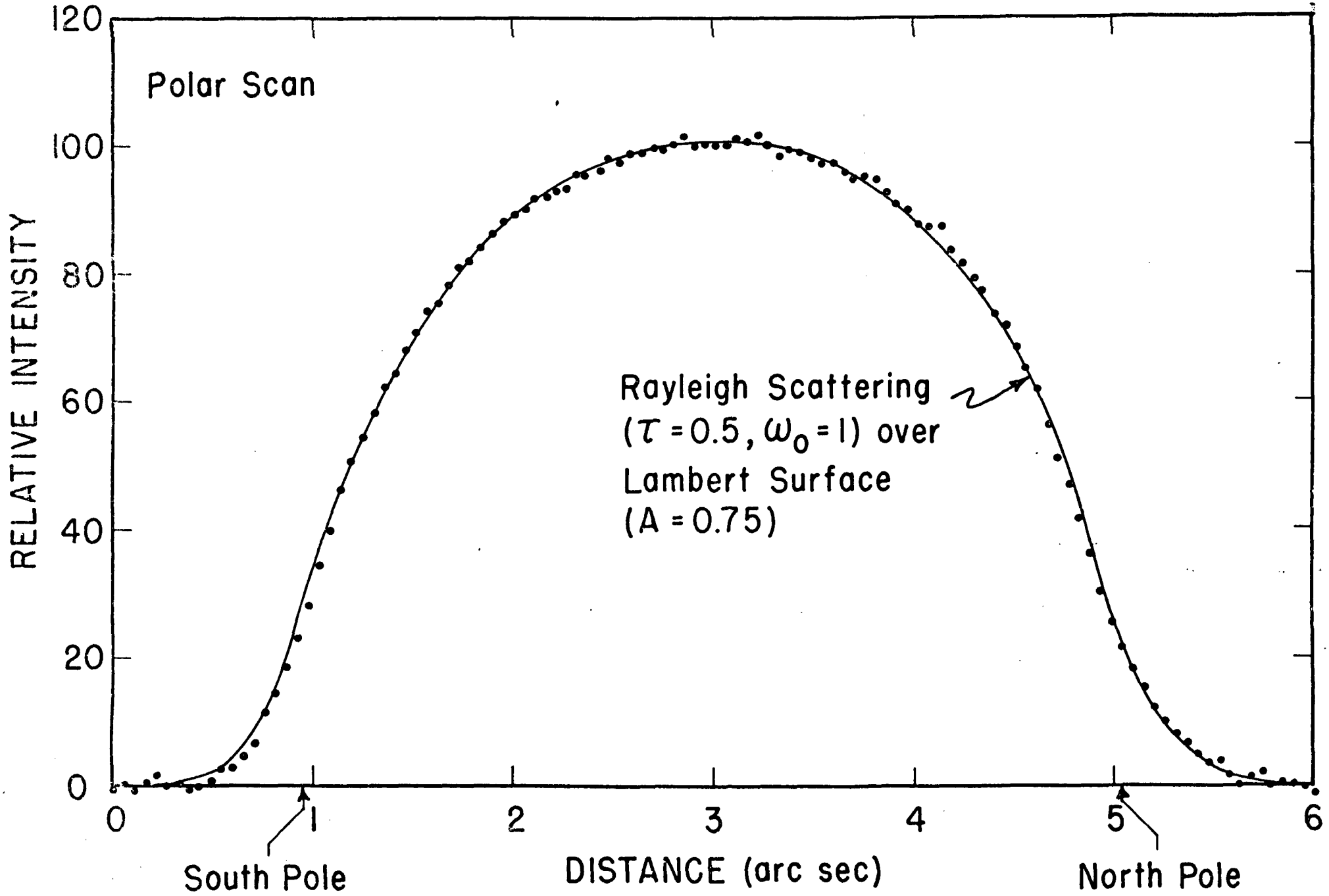
Polar Scan
RELATIVE INTENSITY
120
100
80
60
40
20
0
0
1
2
3
4
5
6
Rayleigh Scattering
($\tau = 0.5, \omega_0 = 1$) over
Lambert Surface
(A = 0.75)
South Pole
DISTANCE (arc sec)
North Pole